Research Article | Open Access

Microstructures

Zhang *et al. Microstructures* **2026**, *6*, 2026080 **DOI:**10.20517/microstructures.2026.20

Tunable self-recoverable near-infrared mechanoluminescence from platelike strontium-aluminate: $SrAl_{12}O_{19}:Cr^{3+}$

Qi'an Zhang[1,#], Ziyi Fang[1,#], Mingzhi Wu[1], Yang Liu[1], Qidong Ma[1], Jiazhen Zhou[1], Shengqiang Liu[1], Dengfeng Peng[1,2,3]

Keywords: Mechanoluminescence, near-infrared, self-recoverable, platelike $SrAl_{12}O_{19}$, sensing and anti-counterfeiting

Citation: Zhang, Q.; Fang, Z.; Wu, M.; Liu, Y.; Ma, Q.; Zhou, J.; Liu, S.; Peng, D. Tunable self-recoverable near-infrared mechanoluminescence from platelike strontium-aluminate: $SrAl_{12}O_{19}:Cr^{3+}$. *Microstructures* **2026**, *6*, 2026080. https://dx.doi.org/10.20517/microstructures.2026.20

Received: 2 Feb 2026 **First Decision:** 3 Mar 2026 **Revised:** 18 Mar 2026 **Accepted:** 23 Mar 2026 **Published:** 12 Jun 2026

Academic Editor: Dae-Yong Jeong **Copy Editor:** Shu-Yuan Duan **Production Editor:** Shu-Yuan Duan

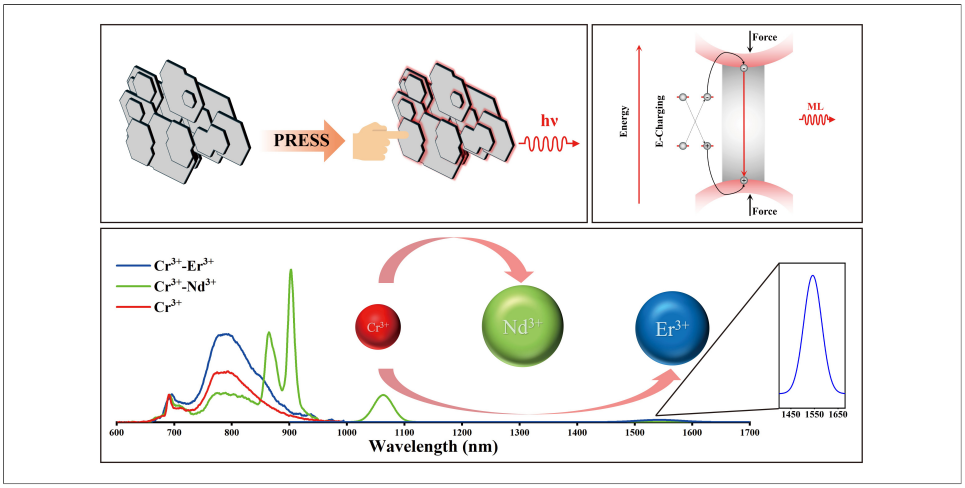

Abstract

The development of high-performance self-recoverable near-infrared (NIR) mechanoluminescent materials is crucial for advancing applications. In this work, we presented a self-recoverable NIR mechanoluminescent material, platelike $SrAl_{12}O_{19}$, through singly doped with Cr^{3+} and co-doped with lanthanide ions (Nd^{3+}, Yb^{3+}, Er^{3+}) in one step. By modulating the Cr^{3+} doping concentration, we achieved precise control over the mechanoluminescence (ML) intensity as well as the spectral tunability between characteristic R-line emission (~ 690 nm) and the broadband emission (750-950 nm). Moreover, energy transfer from Cr^{3+} to lanthanide ions enables multispectral ML emission extending into the NIR-II window (1,000-1,700 nm). The resultant material exhibits excellent ML self-recoverability and high chemical stability. The co-doped system was demonstrated with great potential in dynamic stress visualization, naked-eye-invisible information encryption and special identification under challenging conditions (e.g., underwater). We further demonstrated practical applications by fabricating dual-mode

[1]College of Physics and Optoelectronic Engineering, Shenzhen University, Shenzhen 518060, Guangdong, China.
[2]Key Laboratory of Optoelectronic Devices and Systems of Ministry of Education and Guangdong Province, Shenzhen University, Shenzhen 518060, Guangdong, China.
[3]China State Key Laboratory of Radio Frequency Heterogeneous Integration, Shenzhen University, Shenzhen 518060, Guangdong, China.
[#]These authors contributed equally to this work.

Correspondence to: Prof. Dengfeng Peng, Assist. Prof. Shengqiang Liu, College of Physics and Optoelectronic Engineering, Shenzhen University, Shenzhen 518060, Guangdong, China. E-mail: pengdengfeng@szu.edu.cn; sqliu@szu.edu.cn

flexible NIR mechanoluminescent paper sheets and sprayable coatings. This work contributes to the advancement of new NIR mechanoluminescent materials with unique morphological features for various scenarios, including the advancement of intelligent sensing and multi-level anti-counterfeiting technologies.

INTRODUCTION

Mechanoluminescence (ML) describes the form of light emission that directly responds to dynamic mechanical stimuli[1]. Distinct from traditional forms of light emission - such as photoluminescence (PL), electroluminescence (EL), or reaction-driven processes like chemiluminescence (CL) and bioluminescence (BL)[2], ML can directly convert mechanical energy (e.g., compression, friction, or twisting[3]) into light energy in one step, making it an efficient and clean energy conversion technology[4]. The energy sources for ML behavior are diverse, ranging from kinetic energy generated by human sports activities to natural mechanical energy. Consequently, ML materials hold significant promise for a wide range of applications such as structural health monitoring[5], smart sensors[6] and human-machine interactive interfaces[7]. Specifically, the NIR spectrum presents minimal interference from ambient light, enabling more precise measurements in bright environments. Besides, the NIR spectrum exhibits superior tissue penetration, favorable for *in vivo* imaging applications[8,9]. These characteristics have recently spurred considerable research interest in developing high-performance NIR ML materials. The NIR ML materials can emit beyond the visible spectrum, present promising new solutions to overcome the current ML applications' limitations. Currently, NIR ML materials, such as CaZnOS:Nd^{3+}[10], $LiNbO_3$:Nd^{3+}[11], $LiGa_5O_8$:Pr^{3+}[12] and $SrZn_2S_2O$:Yb^{3+}[13] rely exclusively on rare-earth dopants which manifest high cost and limited spectral tunability of rare-earth elements. Consequently, extensive research has been conducted on Cr^{3+}-activated phosphors, such as $Y_3Al_5O_{12}$:Cr^{3+}[14], $CaAl_{12}O_{19}$:Cr^{3+}[15,16], Ga_2O_3:Cr^{3+}[17,18], $LaAlO_3$:Cr^{3+}[19] and $Lu_3Ga_5O_{12}$: Cr^{3+}[20]. The luminescence of Cr^{3+} is uniquely governed by crystal field strength, enabling a broad tunable emission from approximately 700 to 1,200 nm. This attribute facilitates the development of high-performance NIR ML materials via adjusting the coordination environment of Cr^{3+} ions.

Cr^{3+}-activated NIR ML materials are broadly classified into two categories: trap-controlled and self-recoverable types. Trap-controlled NIR ML materials require pre-irradiation with ultraviolet (UV) light to populate charge carriers in traps prior to ML. After multiple stress cycles, these traps are largely de-trapped, preventing sustained emission. In contrast, self-recoverable NIR ML materials exhibit stable and continuous luminescence upon repeated mechanical stimulation, holding unique potentials for *in vivo* biological imaging[21], rapid stress detection in large-scale structures, and sports biomechanics analysis. Although significant progress has been made in achieving self-recoverable Cr^{3+}-activated ML, research reports on the controlled synthesis with well-defined morphologies are scarce[22-24]. The physical properties of Cr^{3+}-activated ML materials are governed by crystal anisotropy, which also influences the processability and long-term stability in practical applications. Platelike structure possesses highly uniform morphology and excellent substrate compatibility, allowing conformal adhesion to both flat and irregular surfaces. By capturing its NIR ML images, stress distribution across complex components can be obtained intuitively. However, current platelike NIR ML materials are relatively scarce. The predominant synthesis strategies involve secondary processing after a high-temperature solid-state or molten salt shielding synthesis[25], which requires a large amount of solvent to improve morphology with additional washing steps. A preliminary synthesis of Cr^{3+}-doped matrix with varying Sr/Al ratios was conducted to compare their ML intensity and morphological characteristics. $SrAl_{12}O_{19}$ was selected as the ideal matrix, exhibiting superior ML intensity and unique platelike morphology [Supplementary Figures 1-3]. $SrAl_{12}O_{19}$, due to its magnetite structure, exhibits uniform and extensive platelike structures via a single-step high-temperature solid-state reaction[26]. Unlike other irregular particle morphologies that form gaps during accumulation, platelike $SrAl_{12}O_{19}$ can align parallel to the substrate surface, forming dense and continuous layers. These characteristics highlight the

potential of platelike $SrAl_{12}O_{19}$ in advanced NIR ML applications.

In this work, we synthesized a series of platelike $SrAl_{12}O_{19}:Cr^{3+}$ self-recoverable NIR ML samples via a one-step high-temperature solid-state method. First, adjusted the ML intensity by modulating the Cr^{3+} doping concentration, which enables variation between the R-line narrow emissions and broadband wide emissions. Then systematically investigated the ML properties under different synthetic conditions. Furthermore, co-doped with Nd^{3+}, Yb^{3+} and Er^{3+} ions to achieve multi-spectral ML. Based on Cr^{3+} and Nd^{3+} co-doped samples, we designed NIR ML paper sheet and spray coating - for anti-counterfeiting, thereby proposing a novel strategy for the application of NIR ML.

MATERIALS AND METHODS

Preparation of phosphor

A series of $SrAl_{12}O_{19}:x$ mol% Cr^{3+} (x = 0.1, 0.5, 1, 2, 4) phosphors were synthesized via a one-step high-temperature solid-state method. The high-purity raw materials include $SrCO_3$ (99%, Sinopharm Chemical Reagent), Al_2O_3 (99.99%, Sinopharm Chemical Reagent), Cr_2O_3 (99.95%, Aladdin), Nd_2O_3 (99.99%, Aladdin), Yb_2O_3 (99.99%, Macklin), and Er_2O_3 (99.99%, Macklin).

These reagents were weighed according to the stoichiometric ratio and transferred to an agate mortar. An appropriate amount of ethanol was added as a mixing medium. The mixture was thoroughly ground and homogenized until the ethanol largely evaporated. After that, the precursors were subsequently transferred to the forced-air drying oven and set to 80 °C to ensure complete ethanol removal. The dried precursor powder was then loaded into an alumina crucible and sintered in a high-temperature box furnace at 1,250-1,650 °C for 4 h under an air atmosphere. All samples were heated from room temperature to 1,000 °C at a rate of 10 °C/min, and then heated to 1,250-1,650 °C at a rate of 5 °C/min. After holding at 1,250, 1,350, 1,450, 1,550, 1,650 °C for 4 h, the samples were subsequently cooled down naturally within the furnace chamber. Finally, the as-synthesized block samples were ground into fine powder using an agate mortar and passed through a 150-mesh stainless steel sieve for subsequent characterizations and application designs.

Characterization

The phase purity of the synthesized $SrAl_{12}O_{19}:x\%Cr^{3+}$ compounds was analyzed by X-ray diffraction (XRD) using an Ultima IV high-resolution diffractometer (Rigaku Corporation, Japan), with data collected in the range of 10-120°. The Rietveld refinement was performed using the GSAS-II software. The platelike morphology of the samples was captured by a field emission scanning electron microscope (FESEM) on a Gemini SEM 560 instrument (ZEISS, Germany). Elemental analysis was conducted using energy-dispersive X-ray spectroscopy (EDS) with an Oxford cryogenically cooled spectrometer ULTIM MAX (Oxford, UK). Microstructural characterization was performed by aberration-corrected transmission electron microscopy (TEM) on a Titan Cubed Themis G2 300 microscope (Thermo Fisher Scientific, The Netherlands). PL spectra and fluorescence decay curves were measured with an Edinburgh FLS1000 spectrometer (Edinburgh Instruments, UK). Quantum efficiency (QE) was measured with Quantaurus-QY Plus C13534-12 (Hamamatsu Photonics, Japan). The ML experiments were conducted with a custom-built setup including a digital push-pull gauge, a metal slider driven by a linear motor, and an optical fiber connected to the spectrometer. The ML spectra were acquired using an QE65 PRO high-sensitivity spectrometer (Ocean Optics, USA) for the visible range and an NIR QUEST 512 spectrometer (Ocean Optics, USA) for the NIR region. For ML testing, the films were prepared using a PTFE mold (5 × 5 × 0.03 cm) featuring five parallel 10 × 2 mm rectangular sections. The material block was first crushed and sieved through a 150-mesh stainless steel screen to obtain a uniform powder. This powder was then evenly distributed into the mold's rectangular sections. After removing any excess, the shaped powder strips were thermally sealed with PET laminating film to create the final test samples. The ML signal was subsequently obtained by scraping the film surface

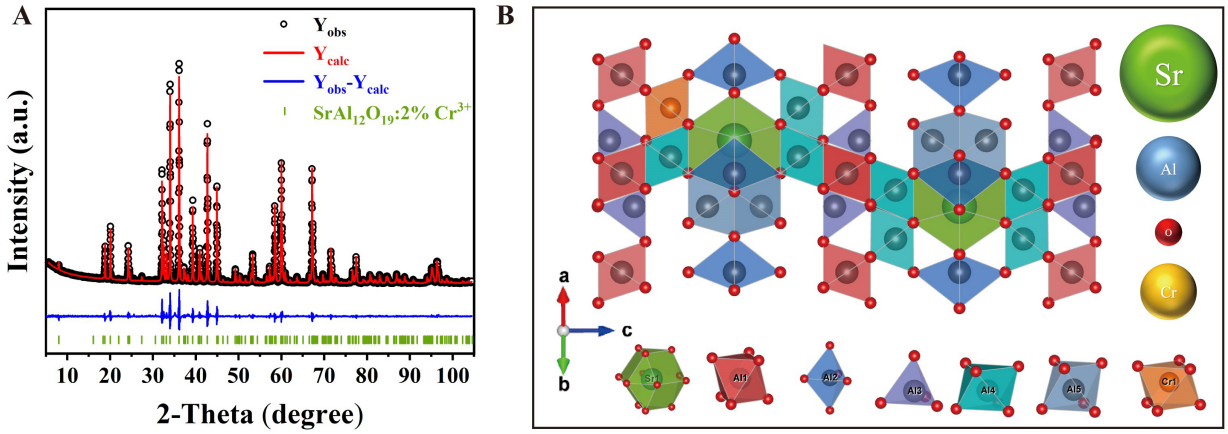

Figure 1. (A) Rietveld refinement of $SrAl_{12}O_{19}$:2%Cr^{3+} synthesized at 1,650 °C; (B) Crystal structure of $SrAl_{12}O_{19}$:Cr^{3+}.

with the metal slider at a distance of 20 mm and a speed of 16 mm/s. The PDMS used in the application section was prepared by mixing powder and PDMS in a 1:1 mass ratio. After being placed in an oven for 6 h, it was cured for subsequent testing. All the NIR images and videos were captured using an ONV3+ night vision device (ORPHA, Germany) and a smartphone. The infrared thermal video was captured by a TI25 instrument (Fluke, USA).

RESULTS AND DISCUSSION

Structure characterization of $SrAl_{12}O_{19}$:*x*%Cr^{3+}

The magnetite-type $SrAl_{12}O_{19}$ matrix belongs to the hexagonal crystal system with a space group of $P6_3/mmc$. Rietveld refinement of the XRD pattern demonstrates an excellent agreement between the calculated (red line) and observed (black circles) data for $SrAl_{12}O_{19}$:2%Cr^{3+} sample [Figure 1A]. The refinement parameters were *Rp* = 5.70%, *Rwp* = 7.85%, and GOF = 2.25. After introducing Cr^{3+} into the host lattice, the unit cell parameters of the $SrAl_{12}O_{19}$:2%Cr^{3+} sample increased ($a = b$ = 5.5685 Å, c = 22.0114 Å) compared with the undoped $SrAl_{12}O_{19}$ matrix ($a = b$ = 5.5666 Å, c = 22.0018 Å). This lattice expansion can be attributed to the replacement of Al^{3+} ions (0.535 Å, CN = 6) by larger Cr^{3+} ions (0.615 Å, CN = 6)[27]. These results provide clear evidence that Cr^{3+} ions successfully replaced Al^{3+} sites in the host structure. Supplementary Figure 4 shows the XRD patterns of $SrAl_{12}O_{19}$:*x*%Cr^{3+} synthesized with varying Cr^{3+} doping concentrations (x = 0, 0.1, 0.5, 1, 2, 4) at 1,650 °C for 4 h. All diffraction patterns remain nearly identical and closely match the standard card of $SrAl_{12}O_{19}$ (PDF#80-1195), confirming the doping of Cr^{3+} does not induce any secondary phases or alter the host crystal structure. Similarly, Supplementary Figure 5 shows the XRD patterns of samples $SrAl_{12}O_{19}$:2%Cr^{3+} synthesized at different sintering temperatures (1,250, 1,350, 1,450, 1,550 and 1,650 °C) for 4 h. At 1,250 °C, several peaks from Al_2O_3 impurity (PDF#88-0826) are evident. However, these peaks are largely eliminated when the temperature reaches 1,350 °C, and a pure $SrAl_{12}O_{19}$ phase is gradually obtained (PDF#80-1195), indicating that a synthesis temperature of 1,350 °C or higher is required to achieve phase-pure $SrAl_{12}O_{19}$ material.

As illustrated in Figure 1B, the crystal structure of $SrAl_{12}O_{19}$:Cr^{3+} comprises one [AlO_4] tetrahedron, one [AlO_5] trigonal bipyramid, and three [AlO_6] octahedra, while the Sr^{2+} occupies the 12-oxygen-coordinated site[28]. The rich crystal structure diversity provides an extremely high compatibility host lattice for doping with various transition metals and rare-earth ions. Furthermore, $SrAl_{12}O_{19}$:Cr^{3+} is composed of alternately stacked mirror-image dense spinel structural units and relatively loose mirror layers. The oxygen ions are densely packed in the spinel structural units but sparsely distributed in the mirror layers[29]. This structural anisotropy promotes preferential crystal growth along the a-b plane, while the large c/a axial ratio (3.95)

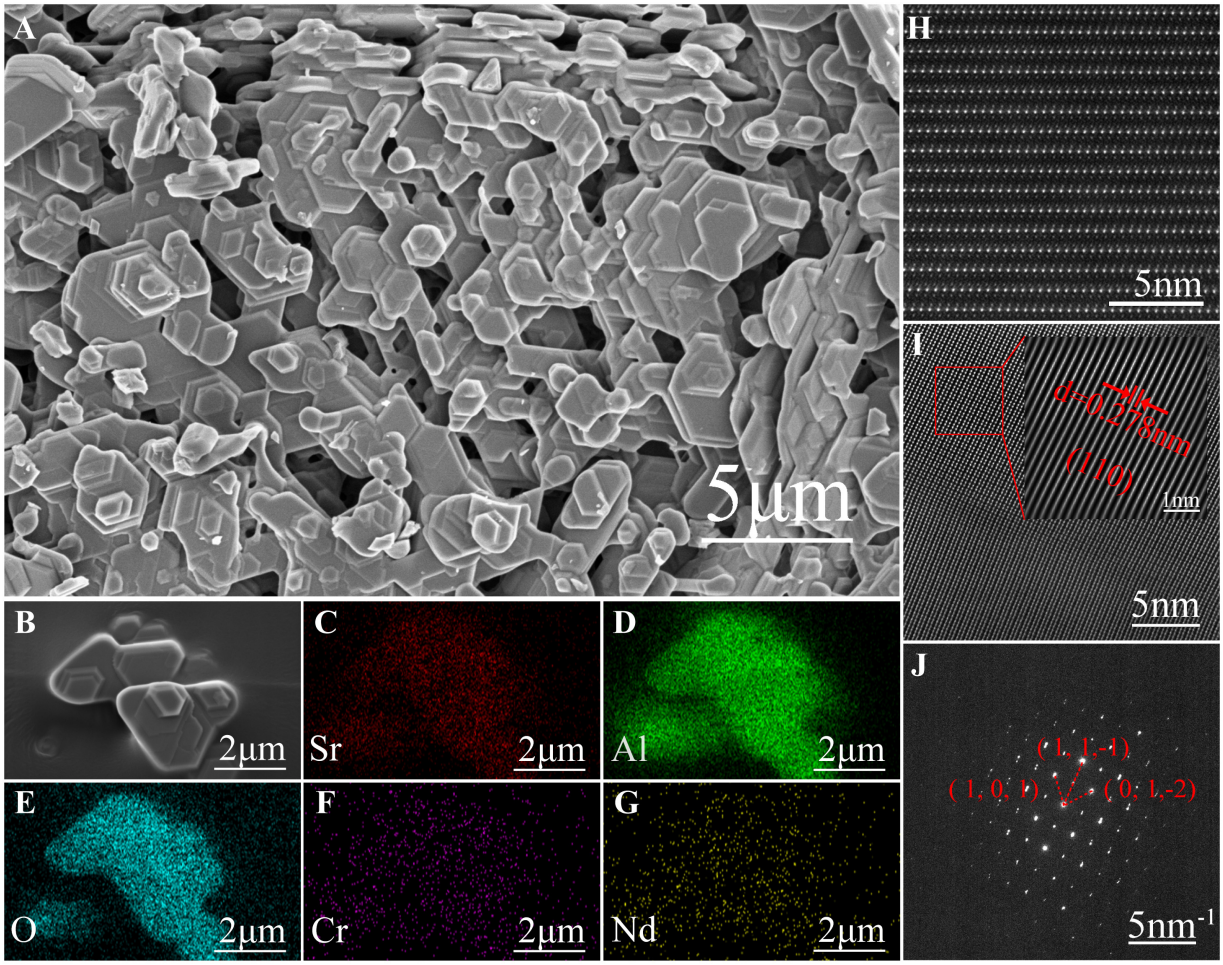

Figure 2. (A) SEM image of $SrAl_{12}O_{19}$:2%Cr^{3+} sample; (B-G) SEM image and element mappings of $SrAl_{12}O_{19}$:2%Cr^{3+}, 1%Nd^{3+} sample; (H) High-resolution TEM image of $SrAl_{12}O_{19}$:2%Cr^{3+}; (I) Fourier transform image of the selected region for $SrAl_{12}O_{19}$:2%Cr^{3+}; (J) Selected area electron diffraction image of $SrAl_{12}O_{19}$:2%Cr^{3+}. SEM: Scanning electron microscope; TEM: transmission electron microscopy.

suppresses growth along the c-axis, ultimately resulting in a stable hexagonal layered structure for $SrAl_{12}O_{19}$:Cr^{3+}[30].

Due to the hydrolysis of the high-performance ML material $SrAl_2O_4$:Eu^{2+}, Dy^{3+}, we specifically conducted comparative experiments and evaluated the aqueous stability of $SrAl_{12}O_{19}$:2%Cr^{3+}. The sample synthesized at 1,650 °C was immersed in deionized water for a month. Afterward, the powder was dried and characterized as shown in Supplementary Figure 6, the XRD pattern of the water-immersed $SrAl_{12}O_{19}$:2%Cr^{3+} sample remains nearly identical to the non-water-immersed sample and the standard card $SrAl_{12}O_{19}$ (PDF#80-1195), with no detectable phase transitions or structural changes. The result indicates the outstanding chemical stability of the $SrAl_{12}O_{19}$:2%Cr^{3+} in aqueous environments, supporting its potential for applications in underwater NIR ML devices. The excellent waterproof performance is intrinsically related to its unique crystal structure.

Morphology of $SrAl_{12}O_{19}$:*x*%Cr^{3+}

To identify the anisotropic growth, Figure 2A presents the SEM image of the $SrAl_{12}O_{19}$:2%Cr^{3+} sample. The result reveals a stacked platelike structure, each comprising multiple single-crystal layers. These platelike morphologies are attributed to the preferential crystal growth along the (001) plane. Notably, the platelike structure of $SrAl_{12}O_{19}$ is achieved through one-step high-temperature solid-state synthesis, eliminating the need for molten salt or secondary processing, thereby offering considerable advantages for NIR ML coating

applications.

Elemental mappings via EDS analysis [Figures 2B-G] confirm the homogeneous distribution of Sr, Al, and O, indicating the successful co-doping of both Cr^{3+} and Nd^{3+} into the $SrAl_{12}O_{19}$ matrix. Figure 2H presents a high-resolution TEM image. Specifically, since Sr atoms present a significantly higher atomic mass than Al atoms, the heavier Sr atoms in the $SrAl_{12}O_{19}$ matrix appear as brighter white spots due to pronounced scattering effects than Al atoms under dark-field conditions. The elemental mappings of the enlarged area in Supplementary Figure 7 further show that Sr, Al, O atoms exhibit a uniform layered distribution, and the Cr atoms are successfully doped into the Al layer. Figure 2I reveals the Fourier transform image, with the corresponding (110) lattice spacing of 0.278 nm. Figure 2J displays the selected area electron diffraction (SAED) pattern of the $SrAl_{12}O_{19}$:2%Cr^{3+} sample. The periodic diffraction spots further indicate a high crystallinity.

PL and ML properties of $SrAl_{12}O_{19}$:*x*%Cr^{3+}

The PL properties of $SrAl_{12}O_{19}$:Cr^{3+} were systematically investigated. Figure 3A presents the photoluminescence excitation (PLE) and PL spectra of $SrAl_{12}O_{19}$:2%Cr^{3+}. The PLE spectrum, monitored at 688 nm emission, exhibits two intense excitation bands centered at 422 and 584 nm, corresponding to the spin-allowed [$^4A_2 \rightarrow {}^4T_1$] and [$^4A_2 \rightarrow {}^4T_2$] transitions of Cr^{3+}. Under excitation at 422 nm, the emission spectrum is characterized by both the R-line and broadband emission. Specifically, the sharp peaks at 688 and 694 nm arise from the spin-forbidden [$^2E \rightarrow {}^4A_2$] transition, and the broadband emission from 750 to 950 nm is ascribed to the spin-allowed [$^4T_2 \rightarrow {}^4A_2$] transition[31]. The co-existence of sharp R-line and the broadband emissions indicates that the Cr^{3+} ions occupy the distorted octahedral sites in the $SrAl_{12}O_{19}$ matrix, with an intermediate crystal field strength[32].

The PLE and PL spectra of $SrAl_{12}O_{19}$:*x*%Cr^{3+} are presented in Supplementary Figure 8. The PL spectra are dominated by sharp R-line emissions at 688 and 694 nm with Cr^{3+} concentration below 1%. As the Cr^{3+} concentration increases, the PL intensity of broadband emission gradually increases and finally surpasses that of sharp emissions. Specifically, the PL intensity reaches a maximum at 1% Cr^{3+} concentration, followed by a concentration quenching with increasing Cr^{3+} concentration. Supplementary Figure 9 presents the PLE and PL spectra of $SrAl_{12}O_{19}$:2%Cr^{3+} synthesized at different temperatures. The PL intensities show monotonic increase as the synthesis temperature is raised. The PL decay curve of $SrAl_{12}O_{19}$: *x*%Cr^{3+}samples are presented in Figure 3B and Supplementary Figure 10 as a function of Cr^{3+} concentration. The corresponding lifetimes were calculated using Equation 1[33].

(1) $$ \tau_{\text {ave }}=\left(A_{1} \tau_{1}^{2}+A_{2} \tau_{2}^{2}\right) /\left(A_{1} \tau_{1}+A_{2} \tau_{2}\right) $$

where A_1 and A_2 are the amplitudes, τ_1 and τ_2 are the decay lifetimes of the individual components, respectively. As a result, the lifetime decreases from 3.22 ms to 0.57 ms as the Cr^{3+} concentration increases. The reduction is attributed to an enhanced probability of energy migration among adjacent Cr^{3+} ions and finally to quenching sites, which collectively promote non-radiative decay pathways. Table 1 summarizes the quantum efficiency measured within 650-950 nm for $SrAl_{12}O_{19}$:*x*%Cr^{3+}. As Cr^{3+} concentration increases, the internal quantum efficiency (IQE) presents a continuous decrease, whereas the external quantum efficiency (EQE) initially increases and then decreases. Notably, the $SrAl_{12}O_{19}$:2%Cr^{3+} sample demonstrates the highest EQE value of 29%.

Consistent with the PL spectra, the ML spectra of $SrAl_{12}O_{19}$:*x*%Cr^{3+} are composed of a sharp R-line emission at 690 nm and a broadband emission spanning 750-950 nm [Supplementary Figure 11]. The sharp R-line corresponds to the spin-forbidden [$^2E \rightarrow {}^4A_2$] transition of Cr^{3+}, whereas the broadband emission arises from

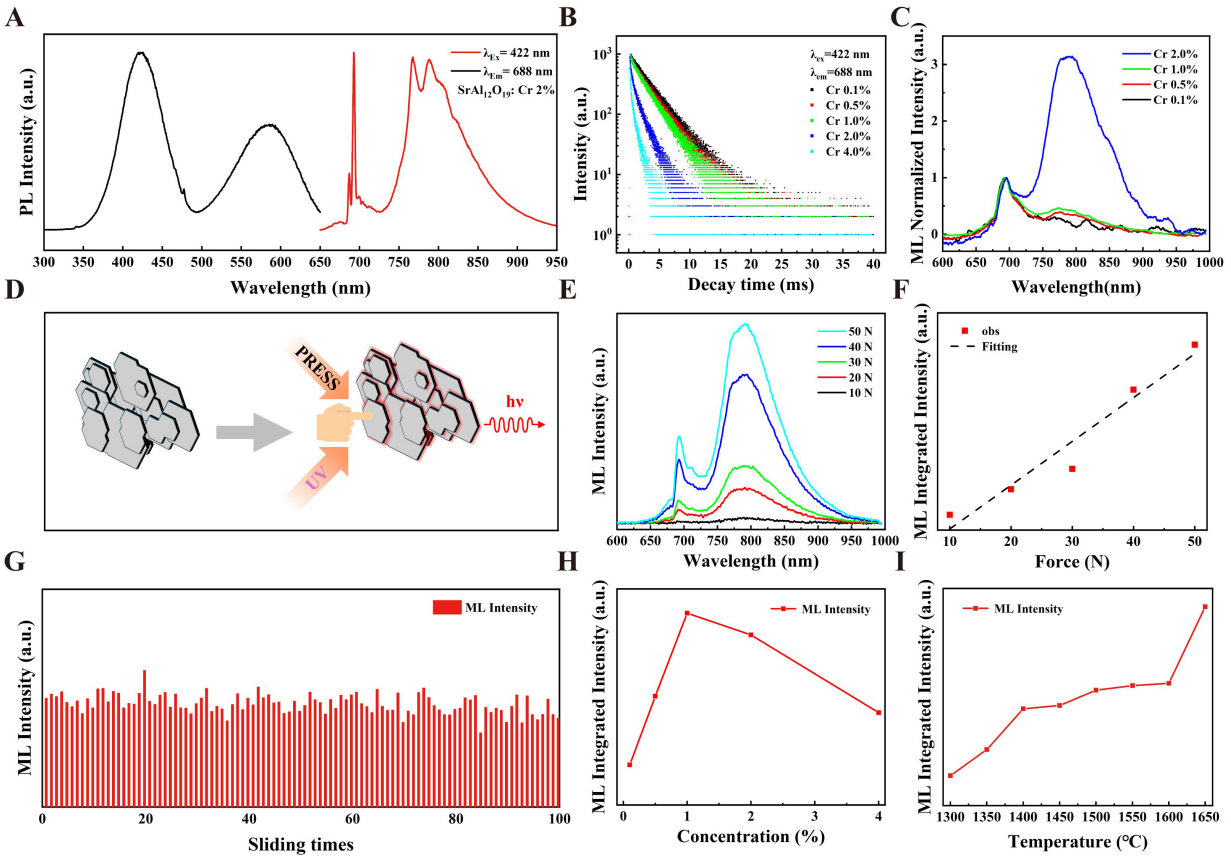

Figure 3. (A) PLE and PL spectra of $SrAl_{12}O_{19}$:2%Cr^{3+}; (B) PL decay curve of $SrAl_{12}O_{19}$:*x*%Cr^{3+}; (C) Normalized ML spectra of $SrAl_{12}O_{19}$:2%Cr^{3+}; (D) Schematic diagram of platelike $SrAl_{12}O_{19}$:*x*%Cr^{3+} NIR luminescence under different stimuli; (E) ML spectra of $SrAl_{12}O_{19}$:2%Cr^{3+} recorded under the applied force from 10 to 50 N; (F) Integrated ML intensity as a function of applied load and corresponding linear fitting; (G) ML Repeatability for $SrAl_{12}O_{19}$:2%Cr^{3+} under periodic load; (H) Integrated ML intensity of $SrAl_{12}O_{19}$:*x*%Cr^{3+} under an applied load of 30 N; (I) Integrated ML intensity of $SrAl_{12}O_{19}$:2%Cr^{3+} synthesis at different temperature. PL: Photoluminescence; ML: mechanoluminescence; PLE: photoluminescence excitation; NIR: near-infrared.

Table 1. Quantum efficiency of $SrAl_{12}O_{19}$:*x*%Cr^{3+} samples under 404 and 422 nm excitation

Concentration	IQE (404 nm)	IQE (422 nm)	EQE (404 nm)	EQE (422 nm)
0.1%	85%	90%	11%	12%
0.5%	85%	85%	19%	19%
1.0%	83%	84%	23%	24%
2.0%	80%	77%	29%	27%
4.0%	53%	52%	24%	24%

IQE: Internal quantum efficiency; EQE: external quantum efficiency.

the spin-allowed [$^4T_2 \rightarrow {}^4A_2$] transition of Cr^{3+}. As shown in Figure 3C and Supplementary Figure 11, the ML intensity of $SrAl_{12}O_{19}$:*x*%Cr^{3+} increases with the Cr^{3+} doping concentration increases from 0.1% to 1.0%, reaching maximum at 1.0%. The enhancement is attributed to the increasing quantity of available Cr^{3+} luminescent centers. At higher Cr^{3+} doping concentrations from 1.0% to 4.0%, the ML intensity decreases due to concentration quenching. The reduced interionic distance between Cr^{3+} ions facilitate enhanced energy migration, which promotes non-radiative energy transfer and consequently diminishes the luminescence efficiency. Furthermore, the spectrum exhibits a concentration-dependent shift: the ML is dominated by the R-line emission at Cr^{3+} concentrations below 1.0%, while the broadband emission becomes predominant at

Cr^{3+} concentrations exceeding 1.0%. This unique spectral shift properties arouse our research interest. The $SrAl_{12}O_{19}$:2%Cr^{3+} sample, in which the sharp peak and broadband intensities are comparable, was selected as the primary subject for further investigation. The dual-mode NIR luminescence of platelike material $SrAl_{12}O_{19}$:*x*%Cr^{3+} were further explored, as schematically shown in Figure 3D. To explore the relationship between applied force and ML intensity, Figure 3E displays the ML spectra of the $SrAl_{12}O_{19}$:2%Cr^{3+} sample under linearly increasing applied loads (F = 10-50 N). The corresponding fitting curve demonstrates a nearly linear correlation between the ML intensity and the applied force (R^2 = 0.95), favorable for stress feedback applications [Figure 3F]. Besides, the self-recoverable property of $SrAl_{12}O_{19}$:2%Cr^{3+} was also verified by subjecting the prepared PET film to 100 sliding cycles under 5 N load, as shown in Figure 3G. The recorded ML signals remained stable throughout the test, demonstrating robust ML cyclic stability, the ML intensity remains at 86% of its average value even after 100 cycles. To eliminate the influence of thermal effects on ML, we recorded the $SrAl_{12}O_{19}$:2%Cr^{3+} PET scraping process using an infrared thermal imaging camera. The results showed no significant heating phenomenon [Supplementary Video 1]. These results indicate that $SrAl_{12}O_{19}$:Cr^{3+} belongs to the category of elastico ML materials. Moreover, the material exhibits exceptional chemical stability, as evidenced by the negligible change in the ML before and after water-immersed [Supplementary Figure 12].

Temperature-dependent ML measurements were also performed, and the result shows that the ML intensity progressively diminishes as temperature increases [Supplementary Figure 13]. This phenomenon is attributed to the enhanced lattice vibrations, which generally promote non-radiative relaxation of excited electrons. The ML integrated intensity as shown in Figure 3H for different Cr^{3+} doping concentrations indicate that excessively high doping concentrations weaken the ML intensity, which is attributed to the concentration quenching effect. Additionally, the effect of different sintering temperatures (1,250-1,650 °C) on the ML intensity for the $SrAl_{12}O_{19}$:2%Cr^{3+} sample is also shown in Figure 3I and Supplementary Figure 14. The result indicates that no ML signal can be detected below 1,250 °C, whereas a continuous enhancement is observed with further increasing temperature. The peak position of the ML emission remains unchanged across temperatures. Furthermore, the holding time during reaction was found to have a negligible impact on the ML intensity and spectral curve [Supplementary Figure 15]. Besides, the $SrAl_{12}O_{19}$:2%Cr^{3+} sample was also sintered in a reducing N_2/H_2 atmosphere and exhibits a slight enhancement in ML intensity [Supplementary Figure 16]. This observation is primarily ascribed to limited oxygen incorporation during synthesis, thereby stabilizing oxygen vacancies, which is favorable for promoting local lattice distortion and constructing piezoelectric potential, leading to enhanced ML performance.

Multispectral ML and energy transfer of $SrAl_{12}O_{19}$:*x*%Cr^{3+}

Figure 4A illustrates a proposed mechanism for the ML process. Although the host lattice of $SrAl_{12}O_{19}$ is centrosymmetric, the doping Cr^{3+} ions and oxygen vacancies result in local structural distortion. Under external mechanical force, an internal piezoelectric field is generated, leading to the separation of electron-hole pairs. These electrons subsequently relax to the valence band maximum and recombine with holes. The released energy in the form of photons excites the Cr^{3+} ions to produce the NIR ML. Furthermore, the incorporation of lanthanide ions (Nd^{3+}, Yb^{3+}, Er^{3+}) enables distinct NIR-Ⅱ ML via efficient energy transfer from the excited Cr^{3+}.

Additionally, for $SrAl_{12}O_{19}$, the Sr^{2+} site is favorable for doping lanthanide ions to construct energy transfer pathway and realize NIR-Ⅱ ML. Therefore, the co-doped and tri-doped $SrAl_{12}O_{19}$:2%Cr^{3+}, 1%Nd^{3+} (or 1%Yb^{3+} or 1%Er^{3+} or 1%Yb^{3+}, 5%Er^{3+}) samples were synthesized to modulate the emission spectra[34,35]. Compared with Cr^{3+} singly doped sample, the co-doped samples present distinct emission at 900/1,050, 977, and 1,524 nm under 422 nm excitation, ascribed to the intra-configurational $^4F_{3/2} \rightarrow {}^4I_{9/2}/{}^4I_{11/2}$, $^2F_{5/2} \rightarrow {}^2F_{7/2}$, and $^4I_{13/2} \rightarrow {}^4I_{15/2}$ transitions of Nd^{3+}[36,37], Yb^{3+}[38], and Er^{3+}, respectively [Supplementary Figure 17]. Besides, the introduction of

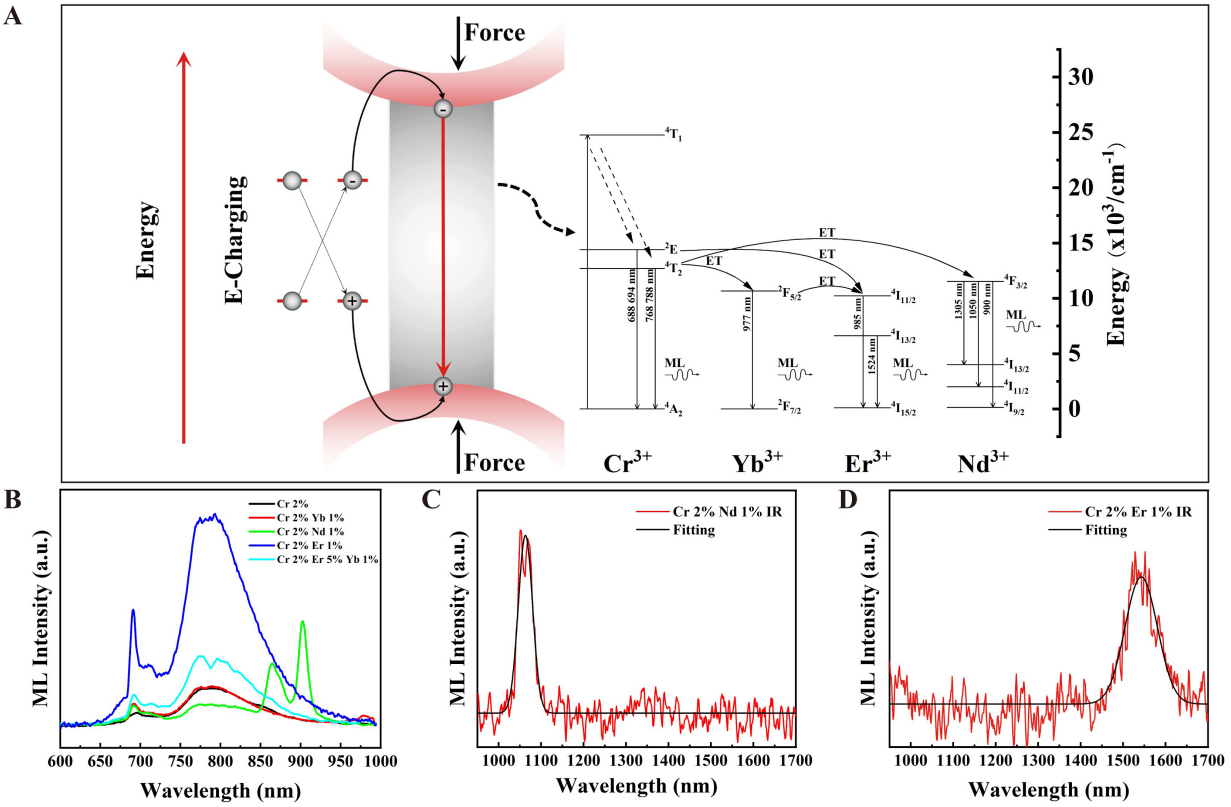

Figure 4. (A) Schematic diagram of the ML mechanism and energy transfer for $SrAl_{12}O_{19}$: Cr^{3+}, Nd^{3+} (or Yb^{3+} or Er^{3+} or Yb^{3+}, Er^{3+}); (B) ML spectra of $SrAl_{12}O_{19}$:2%Cr^{3+}, 1%Nd^{3+} (or 1%Yb^{3+} or 1%Er^{3+} or 1%Yb^{3+}, 5%Er^{3+}) samples employed a visible-NIR detector (600-1,000 nm); (C) ML spectra of $SrAl_{12}O_{19}$:2%Cr^{3+}, 1%Nd^{3+} and (D) ML spectra of $SrAl_{12}O_{19}$:2%Cr^{3+}, 1%Er^{3+} using a NIR detector (900-1,700 nm). ML: mechanoluminescence; NIR: near-infrared.

lanthanide ions leads to reduced luminescence lifetimes [Supplementary Figures 18-21], which provide evidence for energy transfer from Cr^{3+} to lanthanides. Specifically, the lifetime of Cr^{3+}, Nd^{3+} co-doped sample decreases substantially, indicating a significantly higher energy transfer efficiency. The corresponding ML spectra are presented in Figure 4B-D. In contrast to $SrAl_{12}O_{19}$:2%Cr^{3+} sample, the co-doped samples exhibit additional ML emissions within the NIR-II region, which is consistent with the PL spectra. For example, the $SrAl_{12}O_{19}$:2%Cr^{3+},1%Nd^{3+} sample presents pronounced ML emissions at 864, 903 and 1,064 nm, while weak emission ranging 700-900 nm, which can be ascribed to the efficient energy transfer from Cr^{3+} to Nd^{3+} ions. Specifically, the emission at 903 nm, originating from the $^4F_{3/2} \rightarrow {}^4I_{9/2}$ transition, exhibits a doublet structure attributed to the Stark effect. The $SrAl_{12}O_{19}$:2%Cr^{3+}, 1%Yb^{3+} sample presents a significantly weak ML at 980 nm of Yb^{3+} ions, indicating a much weaker energy transfer efficiency from Cr^{3+} to Yb^{3+}. The $SrAl_{12}O_{19}$:2%Cr^{3+}, 1%Er^{3+} sample presents a substantially red-shifted ML at 1,543 nm of Er^{3+} ions. These results collectively demonstrate that the ML spectrum can be effectively tuned via doping lanthanide ions and controlled energy transfer pathways.

Applications of $SrAl_{12}O_{19}$:2%Cr^{3+}, 1%Nd^{3+}

Due to the excellent mechanical-to-photon conversion, ML materials have already been developed for information encryption[39,40], self-powered illumination[41,42], and so on. Leveraging the NIR ML properties of $SrAl_{12}O_{19}$:2%Cr^{3+},1%Nd^{3+}, a dual-mode flexible NIR ML paper was fabricated. The fine powder was homogeneously blended with dehydrated paper pulp block in water at a powder/block mass ratio of 5:1. The mixture was subsequently transferred using a paper-making screen, followed by drying to obtain the final product. Figure 5A and B respectively compare the difference of this paper sheet under ambient light and

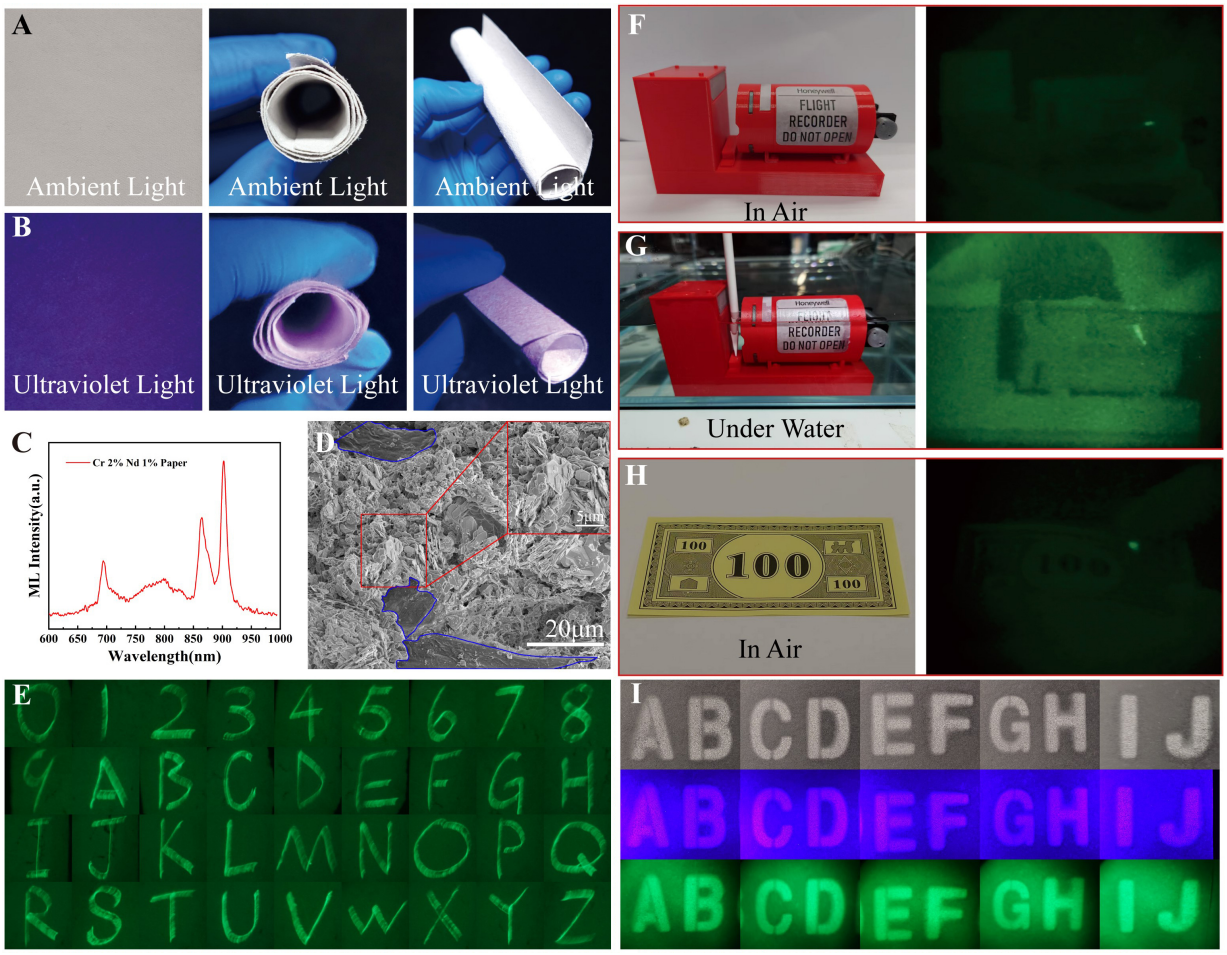

Figure 5. (A) Flexible ML paper sheet made of $SrAl_{12}O_{19}$:2%Cr^{3+}, 1%Nd^{3+} under ambient light; (B) Flexible ML paper sheet made of $SrAl_{12}O_{19}$:2%Cr^{3+}, 1%Nd^{3+} under UV light; (C) ML spectrum of $SrAl_{12}O_{19}$:2%Cr^{3+}, 1%Nd^{3+} ML paper sheet; (D) SEM of $SrAl_{12}O_{19}$:2%Cr^{3+}, 1%Nd^{3+} ML paper sheet (The area outlined in blue is paper fiber.); (E) Under night vision conditions, letters were written on $SrAl_{12}O_{19}$:2%Cr^{3+}, 1%Nd^{3+} ML paper and recorded via time-lapse photography; (F) NIR ML comparison of black boxes in air atmosphere; (G) NIR ML comparison of black boxes under water condition; (H) NIR ML comparison of banknotes; (I) Printed letters with $SrAl_{12}O_{19}$:2%Cr^{3+}, 1%Nd^{3+} sprayer under the condition of ambient light, UV light and night vision. ML: mechanoluminescence; SEM: scanning electron microscope; NIR: near-infrared; UV: ultraviolet.

UV illumination. Under ambient light, the result shows that the resultant paper exhibits off-white bodycolor under ambient light, while dark red PL under UV excitation. Besides, the uniform PL across the paper sheet indicates the homogeneous distribution of the ML powder. A piece of paper sheet was cut and encapsulated in a PET for the ML test. As shown in Figure 5C, the ML spectrum confirms that the paper sheet composite retains the characteristic emission from the pristine $SrAl_{12}O_{19}$:2%Cr^{3+},1%Nd^{3+} powder.

The microstructure of the paper composite was analyzed by FESEM. As shown in Figure 5D and Supplementary Figure 22, the SEM images show the unique platelike morphology with uniform distribution of the $SrAl_{12}O_{19}$:2%Cr^{3+},1%Nd^{3+} sample within the paper fibers of the sheet. The EDS confirmed the presence of all constituent elements [Supplementary Figure 23]. Figure 5E shows a long-exposure image captured with an ONV3+ night vision device, showing the numbers 0-9 and the 26 letters of the alphabet written directly onto the NIR-ML paper sheet using a glass rod. Supplementary Video 2 demonstrates the bending and writing operations performed on the paper sheet in which the NIR ML is clearly captured under night vision device. The paper sheet presents excellent ML repeatability even after 100 sliding experiments [Supplementary Figure 24]. Therefore, this paper exhibits excellent anti-counterfeiting characteristics, as the

written information remains invisible to the naked eye but detectable in the NIR spectrum using specialized equipment.

Besides, the $SrAl_{12}O_{19}$:2%Cr^{3+} phosphor, which exhibits composition and luminescence stability under aqueous environment [Supplementary Figures 6 and 12], shows great potential for applications in underwater NIR ML devices. Accordingly, Figure 5F-H demonstrates the application of this ML coating composed of $SrAl_{12}O_{19}$:2%Cr^{3+} phosphor on various substrates, including black boxes (tested both in air and underwater) and banknotes [Supplementary Videos 3-5]. The ML induced by sand and stone abrasion on the seabed-simulated black box, as well as the ML response from manually scratching the banknotes were simulated. Figure 5I also demonstrates the creation of English letter patterns employing $SrAl_{12}O_{19}$:2%Cr^{3+} 1%Nd^{3+} coating after passing through a perforated plate mask. The patterns were imaged under three conditions: ambient light, UV excitation, and through night vision device with UV excitation. When viewed through night vision device, the intense emission confirms the material's efficient NIR ML capability. Therefore, this dual-mode luminescence - comprising both NIR PL and ML which are only detectable using night vision device under light and mechanical stimulation [Supplementary Video 6] - enables effective application in advanced anti-counterfeiting and specialized marking, significantly enhancing the complexity of information encryption. Additionally, we conducted exploratory ultrasonic testing on PDMS films mixed with $SrAl_{12}O_{19}$:2%Cr^{3+},1%Nd^{3+}. Experimental results demonstrate the material's excellent response to ultrasonic forces, offering new insights for NIR stress luminescence applications within biological organisms [Supplementary Video 7].

CONCLUSIONS

This study presents the development of a platelike $SrAl_{12}O_{19}$ NIR ML material via Cr^{3+} sole-doping and co-doping with rare-earth ions like Nd^{3+}, Yb^{3+}, Er^{3+}. Tunable ML was achieved by modulating the Cr^{3+} doping concentration, which effectively alters the crystal field strength. The introduction of lanthanide rare earth ions further enabled multispectral emission within NIR-Ⅱ region. This material exhibits excellent chemical stability, outstanding self-recoverable properties, and long-term water resistance. Based on the Cr^{3+}, Nd^{3+} co-doped system, NIR ML paper sheet and sprayable coating were designed and demonstrated for applications in information encryption, dynamic response, and special identification. This research provides new insights for expanding the application scenarios of NIR ML materials and advancing smart display technologies.

DECLARATIONS

Acknowledgments

The authors thank Dr. Nan Jian from Electron Microscope Center of Shenzhen University for his help in HRTEM. The authors also acknowledge researcher Mengmeng Ma for assistance from The Photonics Center of Shenzhen University. The authors also thank researcher Yingzhen Li for the assistance on XRD measurements received from the College of Physics and Optoelectronic Engineering of Shenzhen University.

Authors' contributions

Design: Zhang, Q.; Peng, D.
Experiments: Zhang, Q.; Fang, Z.; Wu, M.
Manuscript writing: Zhang, Q.; Liu, S.; Peng, D.
Manuscript revision and supervision: Zhang, Q.; Fang, Z.; Wu, M.; Ma, Q.; Liu, Y.; Zhou, J.; Liu, S.; Peng, D.
All authors reviewed and edited the final version.

Availability of data and materials

The data that supports the findings of this study are available in the Supplementary Materials of this article. Further data are available from the corresponding author upon reasonable request.

AI and AI-assisted tools Statement

Not applicable.

Financial support and sponsorship

This work was supported by the Natural Science Foundation of China (62275170), the Guangdong Provincial Science Fund for Distinguished Young Scholars (2022B1515020054), the Key-Area Research and Development Program of Guangdong Province (2024B0101080001), Shenzhen Fundamental Research Project (JCYJ20240813141624033), Scientific Research Foundation as Phase III construction of high level University 2035 plan (0000050101).

Conflicts of interest

All authors declared that there are no conflicts of interest.

Ethical approval and consent to participate

Not applicable.

Consent for publication

Not applicable.

Supplementary Materials

Supplementary Materials

REFERENCES

1. Chang, S.; Zhang, K.; Peng, D.; Deng, Y.; Shan, C.; Dong, L. Mechanoluminescent functional devices: developments, applications and prospects. *Nano. Energy.* **2024**, *122*, 109325. DOI
2. Schramm, S.; Weiß, D. Bioluminescence - the vibrant glow of nature and its chemical mechanisms. *Chembiochem* **2024**, *25*, e202400106. DOI
3. Wang, J.; Yao, K.; Cui, K.; et al. Contact electrification induced multicolor self-recoverable mechanoluminescent elastomer for wearable smart light-emitting Devices. *Adv. Opt. Mater.* **2023**, *11*, 2203112. DOI
4. Zhou, B.; Liu, J.; Huang, X.; et al. Mechanoluminescent-triboelectric bimodal sensors for self-powered sensing and intelligent control. *Nano-Micro. Lett.* **2023**, *15*, 72. DOI PubMed PMC
5. Shin, H. G.; Timilsina, S.; Sohn, K. S.; Kim, J. S. Digital image correlation compatible mechanoluminescent skin for structural health monitoring. *Adv. Sci.* **2022**, *9*, 2105889. DOI
6. Dong, Y.; An, W.; Wang, Z.; Zhang, D. An artificial intelligence-assisted flexible and wearable mechanoluminescent strain sensor system. *Nano-Micro. Lett.* **2024**, *17*, 62. DOI PubMed PMC
7. Duan, S.; Sang, M.; Chen, H.; et al. Shear stiffening-based mechanoluminescent device for impact-thermal coupling protection and impact visualization. *Adv. Funct. Mater.* **2024**, *34*, 2411821. DOI
8. Jiang, S.; Wu, X.; Yang, F.; Rommelfanger, N. J.; Hong, G. Activation of mechanoluminescent nanotransducers by focused ultrasound enables light delivery to deep-seated tissue *in vivo*. *Nat. Protoc.* **2023**, *18*, 3787-820. DOI
9. Wu, S.; Zhou, G.; Wu, Y.; et al. Multiple defect-induced high-resolution near-infrared mechanoluminescent materials for non-destructive detection of blood glucose and lipids. *Adv. Mater.* **2024**, *36*, 2408508. DOI
10. Li, L.; Wondraczek, L.; Li, L.; et al. CaZnOS:Nd^{3+} emits tissue-penetrating near-infrared light upon force loading. *ACS. Appl. Mater. Interfaces.* **2018**, *10*, 14509-16. DOI PubMed PMC
11. Xiong, P.; Peng, M. Near infrared mechanoluminescence from the Nd^{3+} doped perovskite $LiNbO_3$:Nd^{3+} for stress sensors. *J. Mater. Chem. C.* **2019**, *7*, 6301-7. DOI
12. Xiong, P.; Peng, M.; Qin, K.; Xu, F.; Xu, X. Visible to near-infrared persistent luminescence and mechanoluminescence from Pr^{3+}-doped $LiGa_5O_8$ for energy storage and bioimaging. *Adv. Opt. Mater.* **2019**, *7*, 1901107. DOI
13. Chen, C.; Zhuang, Y.; Tu, D.; Wang, X.; Pan, C.; Xie, R. Creating visible-to-near-infrared mechanoluminescence in mixed-anion compounds $SrZn_2S_2O$ and SrZnSO. *Nano. Energy.* **2020**, *68*, 104329. DOI

14. Liu, Z.; Yu, X.; Peng, Q.; et al. NIR mechanoluminescence from Cr^{3+} activated $Y_3Al_5O_{12}$ with intense zero phonon line. *Adv. Funct. Mater.* **2023**, *33*, 2214497. DOI
15. Tian, B.; Zhao, L.; Wang, Y.; et al. Interfacial charge flow modulation of $CaF_2/CaAl_{12}O_{19}$:Dy heterojunctions for enhanced mechanoluminescence in flexible composites. *Adv. Mater.* **2025**, *38*, e15048. DOI
16. Zhang, Y.; Yu, Y.; Zhao, Q. A three-mode optical thermometer based on Cr^{3+} doped $CaAl_{12}O_{19}$ phosphors. *Ceram. Int.* **2025**, *51*, 7321-9. DOI
17. Suo, H.; Wang, Y.; Zhang, X.; et al. A broadband near-infrared nanoemitter powered by mechanical action. *Matter* **2023**, *6*, 2935-49. DOI
18. Liu, S.; Guo, Y.; Song, Z.; Peng, D.; Liu, Q.; Wang, F. Bright chromium-sensitized lanthanide NIR-II mechanoluminescence in a piezoelectric oxide. *Adv. Mater.* **2025**, *37*, e06957. DOI
19. Shao, P.; Xiong, P.; Xiao, Y.; Chen, Z.; Chen, D.; Yang, Z. Self-recoverable NIR mechanoluminescence from Cr^{3+} doped perovskite type aluminate. *Adv. Powder. Mater.* **2024**, *3*, 100165. DOI
20. Wu, S.; Xiao, B.; Xiao, Y.; Shao, P.; Wang, Y.; Xiong, P. Cr^{3+}-activated broadband near-infrared mechanoluminescence in garnet compound. *Nano. Energy.* **2023**, *116*, 108811. DOI
21. Li, C.; Schramma, N.; Wang, Z.; et al. Ultrasensitive and robust mechanoluminescent living composites. *Sci. Adv.* **2023**, *9*, eadi8643. DOI PubMed PMC
22. Pei, L.; Yu, Y.; Ma, Z.; Wang, X.; Mao, Q.; Zhong, J. Molten salt synthesis of single-crystalline $Sr_2MgSi_2O_7$: Eu^{2+}, Dy^{3+} nanoplates: breaking the afterglow-size trade-off. *Inorg. Chem.* **2025**, *64*, 9084-92. DOI
23. Hu, M.; Yang, W.; Tan, H.; et al. Template-free synthesis of mesoporous and crystalline transition metal oxide nanoplates with abundant surface defects. *Matter* **2020**, *2*, 1244-59. DOI
24. Scarabelli, L.; Sun, M.; Zhuo, X.; et al. Plate-like colloidal metal nanoparticles. *Chem. Rev.* **2023**, *123*, 3493-542. DOI PubMed PMC
25. Tu, D.; Xu, C.; Fujio, Y. Intense red emitting mechanoluminescence from CaZnOS:Mn,Li with c-axis preferred orientation. *J. Adv. Dielect.* **2014**, *04*, 1450017. DOI
26. Vishista, K.; Gnanam, F. Microstructural development of $SrAl_{12}O_{19}$ in alumina-strontia composites. *J. Eur. Ceram. Soc.* **2009**, *29*, 77-83. DOI
27. Shannon, R. D. Revised effective ionic radii and systematic studies of interatomic distances in halides and chalcogenides. *Acta. Cryst. A.* **1976**, *32*, 751-67. DOI
28. Lin, X.; Zhang, R.; Tian, X.; et al. Coordination geometry-dependent multi-band emission and atypically deep-trap-dominated NIR persistent luminescence from chromium-doped aluminates. *Adv. Opt. Mater.* **2018**, *6*, 1701161. DOI
29. Groppi, G.; Cristiani, C.; Forzatti, P. Preparation, characterisation and catalytic activity of pure and substituted La-hexaaluminate systems for high temperature catalytic combustion. *Appl. Catal. B-Environ.* **2001**, *35*, 137-48. DOI
30. Machida, M.; Eguchi, K.; Arai, H. Catalytic properties of $BaMAl_{11}O_{19}$-α (M = Cr, Mn, Fe, Co, and Ni) for high-temperature catalytic combustion. *J. Catal.* **1989**, *120*, 377-86. DOI
31. Tam, T. T. H.; Quang, N. V.; Tu, N.; et al. Promising deep-red emitting Cr^{3+}-doped $SrAl_{12}O_{19}$ phosphors for plant growth LEDs. *Luminescence* **2024**, *39*, e4851. DOI
32. Adachi, S. Review - photoluminescence properties of Cr^{3+}-activated oxide phosphors. *ECS. J. Solid. State. Sci. Technol.* **2021**, *10*, 026001. DOI
33. Meng, X.; Wang, Z.; Huo, X.; et al. Mechanoluminescence and photoluminescence properties of high efficiency near-infrared phosphor and its multifunctional application. *Mater. Today. Chem.* **2025**, *48*, 102893. DOI
34. Verdun, H.; Wortman, D.; Morrison, C.; Bradshaw, J. Optical properties of Nd^{3+} in single crystal $SrAl_{12}O_{19}$. *Opt. Mater.* **1997**, *7*, 117-28. DOI
35. Yan, W.; Chen, Y.; Yin, M. Quenching mechanism of Er^{3+} emissions in Er^{3+} - and Er^{3+}/Yb^{3+}-doped $SrAl_{12}O_{19}$ nanophosphors. *J. Rare. Earths.* **2011**, *29*, 202-6. DOI
36. Dexter, D. L. A Theory of sensitized luminescence in solids. *J. Chem. Phys.* **1953**, *21*, 836-50. DOI
37. Carnall, W. T.; Fields, P. R.; Rajnak, K. Electronic energy levels in the trivalent lanthanide aquo ions. I. Pr^{3+}, Nd^{3+}, Pm^{3+}, Sm^{3+}, Dy^{3+}, Ho^{3+}, Er^{3+}, and Tm^{3+}. *J. Chem. Phys.* **1968**, *49*, 4424-42. DOI
38. Van Pieterson, L.; Heeroma, M.; De Heer, E.; Meijerink, A. Charge transfer luminescence of Yb^{3+}. *J. Lumin.* **2000**, *91*, 177-93. DOI
39. Deng, Y.; Peng, D.; Shen, C. L.; et al. Energy transfer-assisted color conversion of persistent mechanoluminescence in RhB@$SiO_2/SrAl_2O_4$:Eu,Dy system for multilevel information encryption. *Laser. &. Photonics. Rev.* **2024**, *18*, 2400251. DOI

40. Wang, C.; Liu, D.; Wei, G.; et al. Enabling multimodal luminescence in a single nanoparticle for X-ray imaging encryption and anticounterfeiting. *Nano. Lett.* **2024**, *24*, 9691-9. DOI
41. Wu, J.; Zhou, X.; Luo, J.; et al. Stretchable and self-powered mechanoluminescent triboelectric nanogenerator fibers toward wearable amphibious electro-optical sensor textiles. *Adv. Sci.* **2024**, *11*, 2401109. DOI
42. Zhang, X.; Li, Z.; Du, W.; et al. Self-powered triboelectric-mechanoluminescent electronic skin for detecting and differentiating multiple mechanical stimuli. *Nano. Energy.* **2022**, *96*, 107115. DOI